SQUARE-CYLINDER FLOW CHARACTERISTICS MODULATED USING UPSTREAM CONTROL ROD

S. C. Yen * **S. F. Wu**

Department of Mechanical and Mechatronic Engineering
National Taiwan Ocean University
Keelung, Taiwan 20224, R.O.C.

ABSTRACT

The flow patterns, vortex-shedding frequency and aerodynamic performance of the square-cylinder flow were modulated using an upstream control rod. Additionally, the flow behaviors were examined using various Reynolds numbers, rotation angles, and spacing ratios. The flow patterns were visualized using the smoke-wire scheme. The global velocity fields and streamline patterns were analyzed using the particle image velocimetry (PIV). Additionally, the flow modes were characterized based on the kinematics theory. Moreover, the vortex-shedding frequencies behind upstream control rod and the square cylinder were detected using two hot-wire anemometers. The surface pressure on square cylinder was determined using a linear pressure scanner. Then, the aerodynamic parameters were calculated using the surface-pressure profiles. Three characteristic flow modes — single, attached, and bi-vortex-street — were categorized by varying the Reynolds number and spacing ratio. In the attached mode, the position of upstream control rod determined the flow characteristics. Furthermore, in the attached mode, the mean drag force of the square cylinder is about 57% lower than of single-square cylinder.

Keywords: Upstream control rod, Smoke wire, PIV, Vortex shedding.

1. INTRODUCTION

The transient and unsteady flow behaviors occur when flow moves around a bluff body. Therefore, the flow characteristics around the bluff bodies have attracted considerable interest. The unsteady flow behaviors are caused by the pressure gradient and transient flow variations. The pressure gradient and transient flow variations introduce large-scale and periodic flow structures including separation, reattachment bubble, shear-layer instability, and vortex shedding. Accordingly, the control of wake flow has attracted intensive studies. Gad-el-Hak [1,2] systematically elucidated wake-flow characteristics and flow-control mechanism. Namely, the passive and active control methods have been utilized to modulate the flow behaviors. For active flow control, energy is added into the flow fields for modulating the boundary layer and wake flow. These active flow-control schemes include flow injection, flow suction, and acoustic excitations. However, the passive/mechanical flow-control schemes do not require energy inputting into the flow field. The boundary-layer behaviors and wake-flow patterns can be tuned by varying the bluff-body shape.

The unsteady flow structures behind bluff bodies have also attracted considerable interest. Okajima [3] analyzed the vortex-shedding frequency behind rectangular cylinders by varying the aspect ratio and Reynolds number (Re) while $70 < \mathrm{Re} < 2 \times 10^4$. Okajima concluded that the Strouhal number (St) is 0.13 for $10^4 < \mathrm{Re} < 2 \times 10^4$ behind a square cylinder. At an aspect ratio of 2 or 3, the flow pattern changed abruptly and the St-curves are discontinuous. Zdravkovich [4] examined the interference of flow fields between two tandem and two side-by-side circular cylinders. The flow patterns, lift/drag ratios, surface-pressure distributions, velocity profiles, and vortex-shedding behaviors were investigated in various cylinder arrangements. The wake-flow patterns behind two side-by-side circular cylinders were classified as — single vortex streets, biased gap flow, and coupled vortex streets — using various gap ratios. The wake-flow patterns behind two tandem circular cylinders with different spacing ratios were also classified as — single slender body mode, reattachment mode, and binary vortex street mode. Yen *et al*. [5] used PIV method to determine the wake-flow patterns behind two tandem square cylinders. Furthermore, Yen *et al*. classified the flow patterns similar to those defined by Zdravkovich by varying the spacing ratio and rotation angle of square cylinders. Additionally, Yen *et al*. obtained the flow patterns similar to those defined by Zdravkovich.

To characterize the passive flow-control methods, an entity was placed in front of a bluff body to con-

* Corresponding author (scyen@mail.ntou.edu.tw)

DOI : 10.1017/jmech.2012.31
Copyright © 2011 The Society of Theoretical and Applied Mechanics, R.O.C.
https://doi.org/10.1017/jmech.2012.31 Published online by Cambridge University Press

trol/disturb the flow behaviors. Lesage and Gartshore [6] placed a small upstream rod in front of a flat plate, a square cylinder, and a circular cylinder to reduce the dynamic forces acting on the bluff bodies. Moreover, Lesage *et al.* indicated that three methods can reduce the dynamic forces — changing the body shape, altering the structure natural frequency and increasing the structural damping. Additionally, Lesage and Gartshore found that the dynamic forces on the square cylinder were almost independent of Reynolds number. Sakamoto *et al*. [7] indicated that the controlling cylinder can reduce the drag and vibration when this controlling cylinder is installed at satisfactory position outside the shear layer. They also concluded that the forces acting on square cylinder were determined by the shear-layer behavior. Strykowski [8] found that the controlling cylinder suppressed vortex shedding behind the master circular cylinder when the controlling cylinder was placed near the separated shear layer. Zhang *et al.* [9] used an upstream rod to determine the aerodynamic characteristics of a square cylinder. They identified six flow modes by varying the staggered angle and spacing ratio. Moreover, Zhang *et al.* found that drag significantly decreases when the staggered angle is < 20°. Sarioglu *et al*. [10] investigated the dual effect of an upstream controlling rod and the rotation angle (θ) of a square cylinder on pressure distributions and vortex-shedding behaviors. Two flow modes with/without vortex shedding were determined using various spacing ratios. They found that the minimum drag occurs at θ = 0° while spacing ratio is 2.0. Sarioglu *et al*. indicated that this minimum drag is 30% lower than that of the square cylinder without the rod. The drag coefficient (C_D) declined considerably as spacing ratio is above 2.7 and θ falls below 10°. Lesage and Gartshore [11] utilized a small rod in front of a bluff body to investigate the effect of small rod on the flow field and fluid force reduction. They used three bluff bodies — a flat plate, a square and a circular cylinder — behind the small rod. Lesage *et al*. found that two flow regimes (Regimes A and B) were observed around the three bluff bodies. The typical spacing ratio to distinguish these two regimes is around $L/D = 2$, where L denotes the longitudinal spacing from the rod center to the upstream edge of the main body and D represents the frontal width of the main body. On the square cylinder, the reduction of drag is up to 70% with comparing that of a single square cylinder.

The current study attempted to reduce drag by using an upstream controlling rod installed in tandem with a square cylinder. The arrangement of the upstream controlling rod and square cylinder was adjusted to control the boundary-layer separation. The upstream controlling rod induced large-scale change in the flow field. Namely, the controlling rod affected the aerodynamic forces and wake-vortex characteristics. The objects of this investigation were — (1) elucidating the interaction between the controlling rod and the square cylinder, (2) visualizing the flow patterns using the smoke-wire scheme and particle image velocimetry (PIV), (3) analyzing the flow structures using kinematic analysis, (4) evaluating the mean drag and mean lift coefficients using the measured surface-pressure profiles and (5) probing the vortex-shedding frequency using hot-wire anemometry.

2. EXPERIMENTAL SETUP

Figure 1 shows the experimental setup conducted in an open-loop wind tunnel. The dimensions of test section are 50 × 50 × 120cm (width × height × length). The free-stream turbulence intensity is < 0.4% while $0.56 < u_\infty < 45$m/s, where u_∞ is the free-stream velocity. Free-stream velocity was monitored by a Pitot tube connected to a U-tube manometer. The uncertainty of u_∞ is approximately < 3% when a synchronized micro-pressure system and a Pitot tube were aligned carefully. The non-uniformity of average-velocity profile across the test section is < 0.5%. Furthermore, a polished aluminum-alloy plate was set as the test-section floor and three highly transparent acrylic panels were installed as the ceiling and side walls for photography and visualization.

2.1 Square Cylinder and Upstream Controlling Rod

The square cylinder was manufactured from an acrylic bar with sharp edges. The dimensions of square cylinder are 50 × 3 × 3cm (length × width × height). Therefore, the aspect ratio is 16 with referencing the results of West and Apelt [12]. The upstream controlling rod is 0.8cm in diameter and 50cm in length. The inset of Fig. 1 shows the arrangement of the master square cylinder and controlling rod.

2.2 Smoke-Wire Scheme

The flow patterns were visualized using the smoke-wire scheme which was adopted in Yen and Hsu [13]. Two zigzag tungsten wires (diameter = 0.3mm) were installed in the test section. Specifically, one tungsten wire was placed in front of the upstream controlling rod, and the other tungsten wire was installed behind the square cylinder. The zigzag structure was used to control the thickness of smoke streaks and the spacing

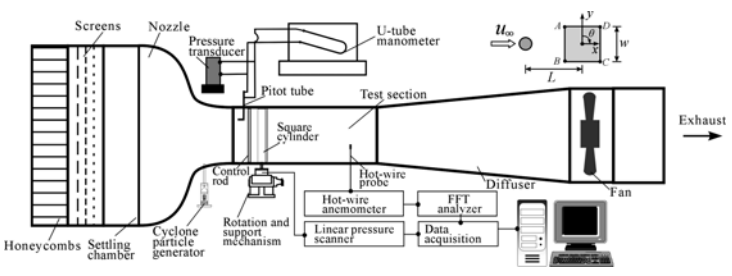


Fig. 1 Visualization wind tunnel

https://doi.org/10.1017/jmech.2012.31 Published online by Cambridge University Press

between two smoke-streak pathlines. A mineral-oil layer was brush-coated thinly on the tungsten-wire surface. The mineral oil was then electrically heated to generate a plain smoke-streak field. The Reynolds number based on the tungsten-wire diameter was maintained at < 40 to prevent vortex shedding behind the wire [14]. The Malvern 1600C Laser Particle Analyzer indicated that the oil-aerosol diameter is 1.7 ± 0.3μm. Therefore, for $1.8 < u_\infty < 9.8$m/s, the Stokes number [15] is located in the range of 3.24×10^{-4} to 1.76×10^{-3}, which is much lower than 1. Stokes number was defined as $Stk = \tau u_\infty / w$, where τ is the relaxation time for oil aerosols ($\tau = 3.6 \times 10^{-6}$ sec) [15], and w is the width of square cylinder. Consequently, the Stokes numbers indicated that the smoke streaks properly followed the flow. Finally, the smoke streaks were illuminated with a 0.5-mm-thick laser-light sheet focused on the mid-plane of the square cylinder. The smoke-streak images were recorded at a frame rate of 30 frames/s (fps) using a CCD camera and a high-quality image grabber.

2.3 PIV Measurement

The PIV image acquisition system included two pulse diode lasers, a high speed camera, and a time-synchronization control system. The herein setup of PIV system was adopted from Yen and Hsu [13]. The polyamide (PM) particles were emitted from a cyclone generator in the open-loop wind tunnel. The maximum energy of laser beams emitted from the two pulse diodes was 6 watts. The laser beams were transmitted through an optical fiber and then connected to a 20° laser-light-sheet expander. The laser expander was mounted on the side rod of outer steel frame. The thickness of the laser-light sheet was adjusted to about 0.5 mm and then aligned with the mid plane of the square cylinder. To grab the image, the particle images were recorded using an IDT Model XS-4 CCD camera (resolution = 512 × 512 pixels). The camera pixels are 16 microns square and the camera could operate continuously or in external trigger mode. The pixel array was zoomed and mapped to a physical region of approximately 13 × 13cm^2. Therefore, spatial resolution is around 254μm/pixel. The CCD camera had a maximum frame rate of 5145 frames/s (fps) and the exposure times is 0.2ms. Each frame consists of two interlaced video fields (even and odd) with a time interval of 1/5145s.

The PIV post-processing system includes an image interrogation system and post interrogation system. Two consecutive image frames were analyzed using the cross-correlation method developed by Keane and Adrian [16]. This algorithm was embedded in VidPIV4 software obtained from Optical Flow Systems. The VidPIV4 software (Optical Flow Systems) used the same approach to calculate the mean displacement of local particle groups between two consecutive images. Additionally, the interrogation window was set using 32 × 32 pixels. To reduce the velocity bias in the regions of large velocity gradients, the ratio of the displacement between the frame images to the length of interrogation area was maintained below 1/4, as suggested by Keane and Adrian [17]. Filtering and interpolation were used to identify outliers and then to regenerate the missed data points. The global filter finds all globally inconsistent data while the local filter finds those that may be globally consistent but inconsistent with the local variations in the vector magnitude and direction.

This interpolation method is based on the weighted-mean technique which replaces the values at the filtered sites in an iterative manner by replacing those with the most surrounding valid values first, working toward those that are less favorably positioned, for accurate and reliable interpolation. Adaptive cross-correlation, employing smaller interrogation size and smaller grid spacing, is finally applied to the vector field generated from the regular procedure of cross correlation, filtering (global and local), and interpolation to provide higher resolution and accuracy than the first pass. A series of instantaneous vector fields are required to calculate the ensemble averages. Mean velocity properties can be obtained by combining a sufficient number of vector fields . The measurement uncertainty (U) was estimated by Abernethy *et al.* [18]. For instance, the uncertainty with a 95% confidence level is derived as follows: $U = \left[B^2 + (tS_{\bar{x}})^2 \right]^{1/2}$, where B is the bias error, $S_{\bar{x}}$ is the precision index of average, and t is the Student distribution (t = 2 for large samples). The bias error is estimated from the calibrated data and the previous experimental judgment. In addition, the precision index of average is also computed from the random error of measured data. Hence, the uncertainty in the velocity measurements is approximately 4.8%.

2.4 Pressure Transducer

Thirty-two pressure taps were distributed around the mid-plane of the square cylinder. The diameter of pressure tap is 1mm and the spacing between two adjacent taps is 0.8mm. Thirty-two short stainless steel tubes were tightly inserted into each pressure-tap hole inside the hollow square cylinder and then connected to plastic polyester tubes. Surface pressure was measured by a pressure transducer (Setra Co., Model 264) with a maximum measurable pressure of ±1245N/m^2 (accuracy = ±1.0%). The digital controller was used to control the pressure scanner. A PCL-818L-12 data-acquisition card (Advantech Co.) was utilized to convert detected voltages to the pressure signal. The sampling length, sampling rate, and elapsed time were 5000 samples, 250 samples/s and 20s, respectively.

2.5 Hot-Wire Anemometry

The vortex-shedding behaviors were analyzed with a hot-wire probe (TSI 1210-T1.5) and an FFT analyzer (ONO SOKKI Co., Model CF-920). The diameter and length of the hot wire were 5μm and 1.5mm, respectively, to ensure a dynamic response between 15 and 25kHz. The hot-wire signals were fed simultaneously

https://doi.org/10.1017/jmech.2012.31 Published online by Cambridge University Press

into an FFT analyzer and a high-speed PC-based data-acquisition system. The sampling frequency was 16kHz, and the estimated uncertainty of the vortex-shedding frequency was < 0.75%.

3. RESULTS AND DISCUSSION

3.1 Smoke-Streak Flow Patterns and Characteristic Flow Patterns

The smoke-wire scheme was adopted to visualize the detailed structure of complex flow phenomena. The smoke-wire scheme combined high-speed photography with video to visualize flow separation and vortex evolution. The flow patterns around a bluff body varied with the Reynolds number and rotation angle. This study defined Reynolds number (Re) as $\mathrm{Re} = u_\infty w/\nu$, where ν is the kinematic viscosity of air, and w is the width of square cylinder.

Figure 2 shows the smoke-streak flow structures around the controlling rod and square cylinder when Re = 3,715 and θ = 0°. Figures 2(a), 2(c), and 2(e) present the near-field of flow patterns around the square cylinder while Figs. 2(b), 2(d), and 2(f) present the far-field wake structures behind the square cylinder. The flow patterns were altered by changing the spacing ratio (L/w), where L is the center-to-center distance between the upstream controlling rod and the square cylinder. Figure 2(a) shows that the free-stream separated from the controlling rod before impinging on Face AB. The positions of vertices A to D are displayed in the inset of Fig. 1. Furthermore, the shear layer separated at vertices A and B, and therefore vortex shedding occurred behind the square cylinder. The flow configurations at $0 \le L/w \le 1.43$ were defined as single mode. Figure 2(b) indicates that the lateral spacing (a) between successive vortices in the same train is 1.33 cm, and the transverse spacing (b) between two vortex trains is 0.32 cm. Thus, the Karman coefficient (b/a) is 0.24 in this investigation. Levi [19] proved the universal Strouhal law of $b/a = 2St$ which was proposed by Roshko [20] and Bearman [21]. Figure 2(c) presents the smoke-streak flow patterns for $1.43 < L/w \le 2.93$. The free stream separated from the controlling rod and then attached on Faces AD and BC. In this study, this flow pattern was designated] the *attached mode*. Figure 2(d) indicates that a = 1.08cm and b = 0.43cm. Therefore, Karman coefficient is 0.4. Figure 2(e) also shows the flow patterns for $L/w \ge 2.93$, the free stream separated from the controlling rod, and a von Karman vortex formed behind the controlling rod. The separated shear layer impinged on Face AB and then separated from vertices A and B. Finally, vortex shedding occurred behind the square cylinder. Therefore, this flow pattern was called the bi-vortex-street mode. Figure 2(f) reveals that flow separated behind the square cylinder, and a = 1.08cm and b = 0.43cm. Therefore, the Karman coefficient is 0.25.

Figure 3 presents the smoke-streak flow structures when Re = 3,715. Figures 3(a), 3(c), 3(e), 3(g), 3(i) and 3(k) present the near-field of flow patterns around

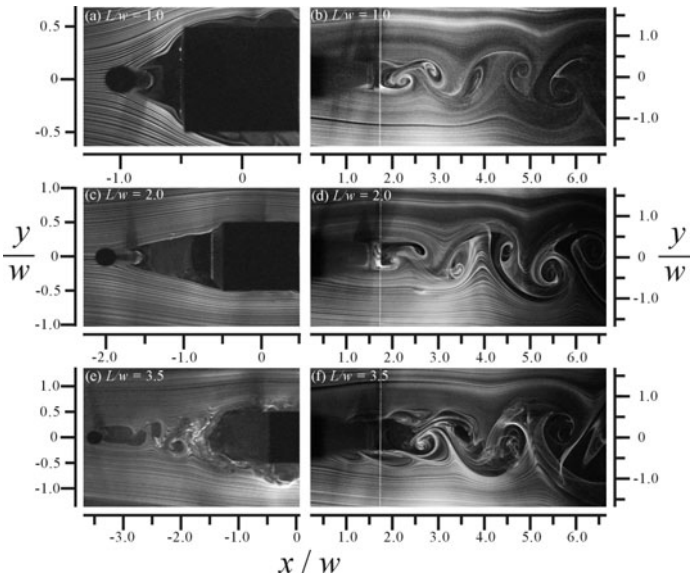


Fig. 2 Profile-view of smoke-streak flow patterns at Re = 3,715 and θ = 0°. Exposure time: 1/2000s

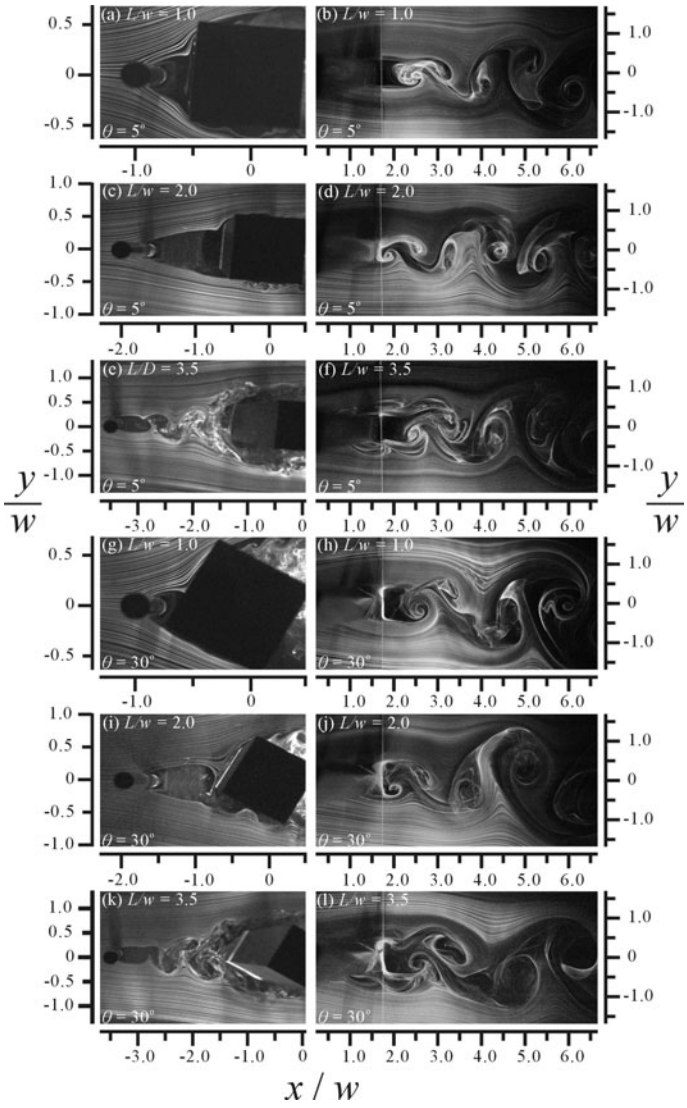


Fig. 3 Profile-view of characteristic smoke-streak flow patterns with various spacing ratio and rotation angle at Re = 3,715. Exposure time: 1/2000s

https://doi.org/10.1017/jmech.2012.31 Published online by Cambridge University Press

the square cylinder while Figs. 3(b), 3(d), 3(f), 3(h), 3(j) and 3(l) present the far-field wake-flow structures behind the square cylinder. The flow patterns were altered by varying L/w and θ. Figures 3(a) and 3(b) show the flow structures at $L/w = 1.0$ for $1° < \theta < 11.5°$. The free stream separated from the controlling rod and then impinged on Face *AB*. The separated shear layer induced a vortex shedding behind the square cylinder. This flow pattern was defined as Mode I. Figures 3(c) and 4(d) display the flow pattern at $L/w = 1.0$ for $11.5° < \theta < 45°$. The shear layer separated from the controlling rod and then attached to Face *BC*. Moreover, the shear layer on Face *BC* separated at vertex *C* and induced a pair of vortices in the wake. This flow pattern was designated Mode II. Figures 3(e) and 3(f) present the smoke-streak flow pattern at $L/w = 2.0$ for $1° < \theta < 9°$. This flow structure resembled that in Mode II. Furthermore, Figs. 3(g) and 3(h) display the flow structures at $L/w = 2.0$ for $9° < \theta < 45°$. The shear layer separated from the controlling rod and then impinged on Faces *AB* and *BC*. Then, the shear layer separated at vertices *A* and *C*. This flow pattern was called Mode III. Figures 3(i) and 3(j) show the flow pattern at $L/w = 3.5$ for $1° < \theta < 12.5°$. A typical von Karman vortex developed behind the controlling rod before impinging on Face *AB*. Furthermore, the shear layer separated at vertices *A* and *B* and then this separated shear layer induced the wake vortex. This flow pattern was designated Mode IV. Figures 3(k) and 3(l) present the smoke-streak flow structures at $L/w = 3.5$ for $12.5° < \theta < 45°$. Specifically, a typical von Karman vortex developed behind the controlling rod and then impinged on Faces *AB* and *BC*. Moreover, the shear layer separated at vertices *A* and *C* and then induced the downstream vortex. This flow pattern was called Mode V.

Figure 4 presents the distribution of characteristic flow modes classified using smoke-streak visualization, as shown in Figs. 2 and 3. Figure 4(a) displays the mode distribution obtained using a controlling rod and a square cylinder without rotation with considering the effects of Reynolds numbers and spacing ratios. Figure 4(a) reveals that the spacing ratio is the dominant factor in controlling the flow-mode distribution. The single, bi-vortex-street, and attached modes occurred at low, high, and moderate L/w, respectively. Figure 4(b) shows the distribution of five characteristic modes using various L/w and θ while Re is fixed at 3,715. The borders that separated different characteristic flow modes had some uncertainties. The maximum ambiguity in identifying different flow modes is approximately ±0.5 for θ, ±0.1 for L/w, and ±50 for Re.

3.2 Vector and Streamline Patterns

The PIV scheme was utilized to measure the ensemble-averaged velocity vectors and streamline patterns. Figures 5 and 6 present the ensemble-averaged streamline patterns using $L/w = 1.0$, 2.0 and 3.5 while Re = 3,715. In Figs. 5 and 6, the streamlines delineate the detailed evolutionary processes of flow structures. The streamline patterns indicate that the vortex-shedding motions are consistent with the smoke-streak

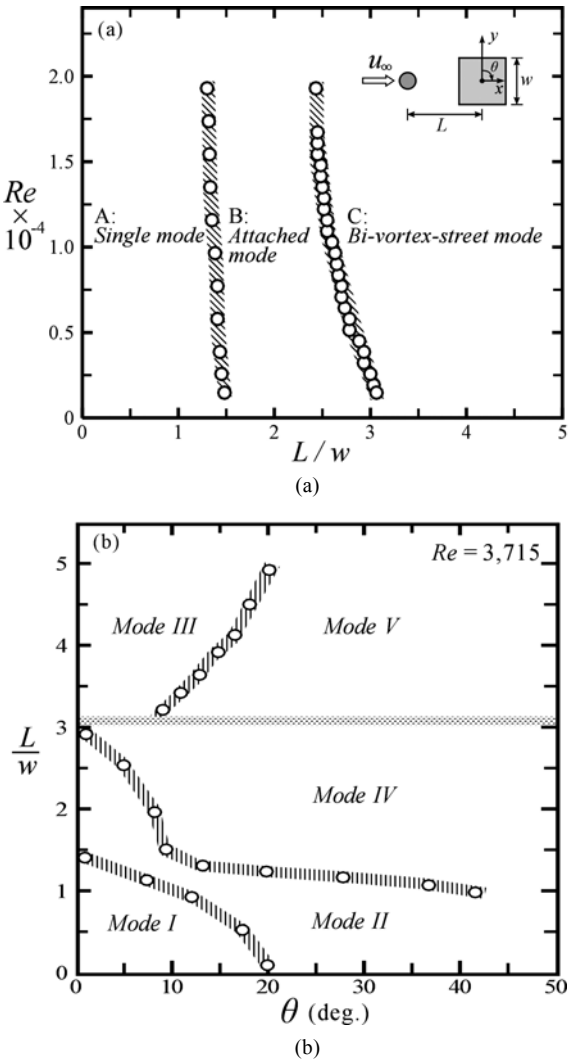


Fig. 4 Distribution of characteristic flow mode. (a) Reynolds number (Re) versus spacing ratio (L/w) at θ = 0°. (b) Spacing ratio (L/w) versus rotation angle (θ) at Re = 3,715

photographs (Figs. 2 and 3). Figure 5(a) reveals that the free stream separated from the control rod and then pounded on Face *AB*. Furthermore, the shear layer separated at vertices *A* and *B*, and a pair of recirculation nodes existed at $(x/w, y/w) \approx (1.4, \pm 0.45)$ behind the square cylinder. Consequently, the flow configurations at $L/w = 1.0$ and θ = 0° are designated the single mode. The flow characteristics in single mode are similar to those of the smoke-streak flow pattern in Fig. 2(a). Figure 5(b) displays the flow pattern when $L/w = 2.0$. The free stream separated from the control rod and then attached on Faces *AD* and *BC*. A pair of recirculation nodes occurred at $(x/w, y/w) \approx (1.6, 0.35)$ and $(2.4, -0.9)$. This flow pattern is designated the attached mode, which resembled that shown in Fig. 2(b). Figure 5(c) indicates that the free stream separated from the control rod, and a von Karman vortex developed behind the control rod as $L/w = 3.5$. Specifically, the contour of von Karman vortex was plotted using the velocity deviation between free stream and vortex [22]. This flow pattern is similar to that shown in Fig. 2(c). Accordingly, this flow pattern is called the bi-vortex- street mode.

https://doi.org/10.1017/jmech.2012.31 Published online by Cambridge University Press

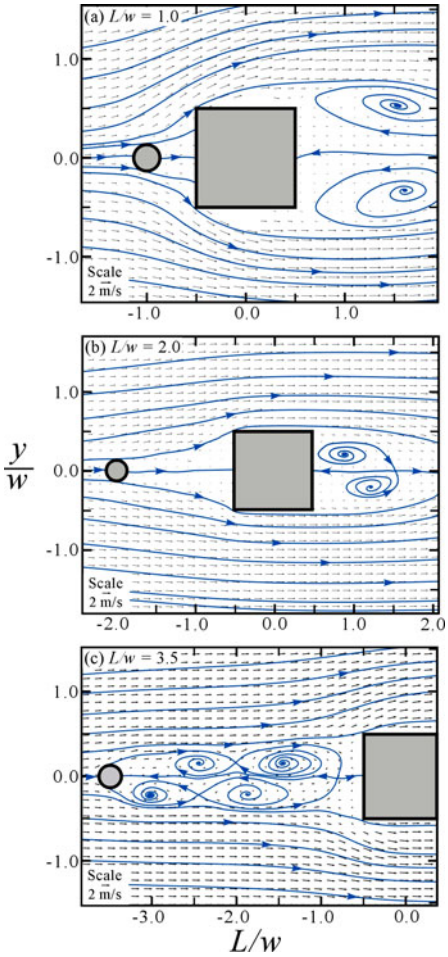


Fig. 5 Velocity vector fields and streamline patterns: (a) single mode at L/w = 1.0, (b) attached mode at L/w = 2.0, and (c) bi-vortex-street mode at L/w = 3.5 while Re = 3,715

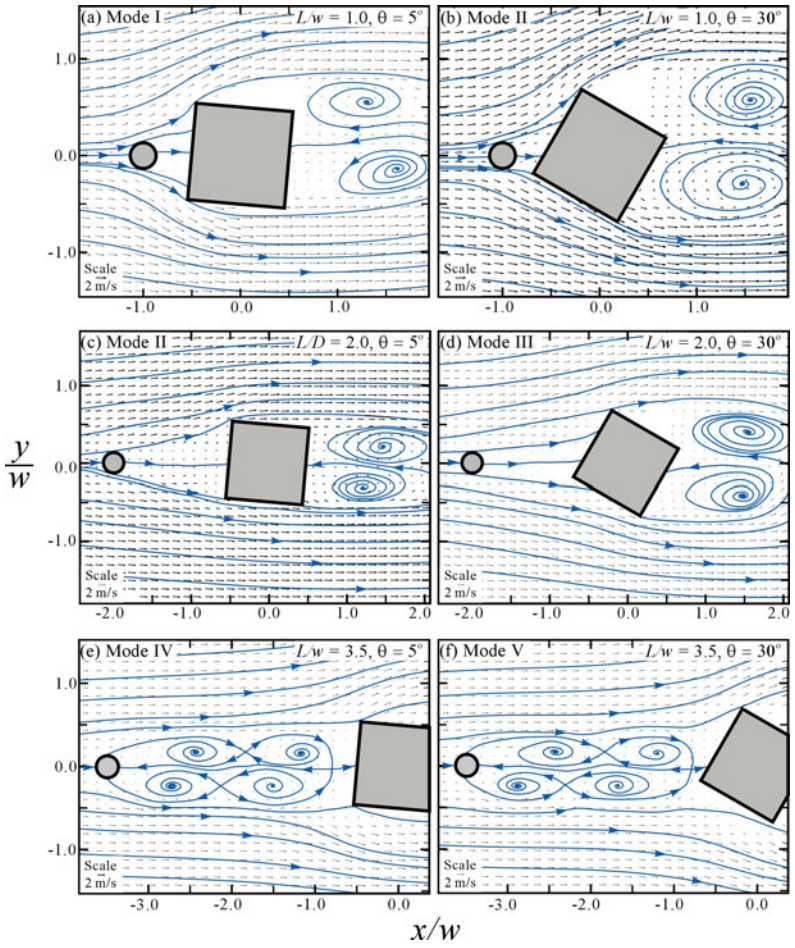


Fig. 6 Velocity vector fields and streamline patterns: (a) L/w = 1.0 at θ = 5°, (b) L/w = 1.0 at θ = 30°, (c) L/w = 2.0 at θ = 5°, (d) L/w = 2.0 at θ = 30°, (e) L/w = 3.5 at θ = 5°, and (f) L/w = 3.5 at θ = 30° while Re = 3,715

Figures 6(a) displays the PIV-flow pattern at θ = 5° and L/w = 1.0. The free stream separated from the upstream control rod and then impinged on Face *AB*. A pair of recirculation nodes occurred at (x/w, y/w) ≈ (1.6, 0.35) and (2.4, −0.9). This flow pattern resembles that shown in Fig. 3(a). Therefore, this flow pattern is named the Mode I. Figures 6(b) and 6(c) present the flow patterns at θ = 30° as L/w = 1.0 and at θ = 5° as L/w = 2.0, respectively. The shear layer separated from the upstream control rod and then attached on Face *BC*. Then, the shear layer separated at vertex *C* and formed a pair of vortices in the wake. These flow patterns resemble those displayed in Figs. 3(b) and 3(c). Consequently, these flow patterns are designated as Mode II. Figure 6(d) presents the flow structure while θ = 30° and L/w = 2.0. The shear layer separated from the upstream control rod and then impinged on Faces *AB* and *BC*. Then, the shear layer separated at vertices *A* and *C*. This flow pattern is similar to that shown in Fig. 3(d). Therefore, it is designated Mode III. Figure 6(e) shows the flow pattern as θ = 5° and L/w = 3.5. The vortex shedding occurred between the control rod and square cylinder. This flow pattern is similar to that displayed in Fig. 3(e). Therefore, it is nominated as Mode IV. Figure 6(f) shows the flow pattern at θ = 30° and L/w = 3.5. The vortex shedding occurs between the control rod and square cylinder; and then impinges on Faces *AB* and *BC*. This flow pattern resembles that presented in Fig. 3(f). Therefore, it is designated Mode V.

3.3 Kinematic Analysis

Figures 7 and 8 present the kinematic flow structures. The analysis scheme of kinematic flow was developed by Perry and Fairlie [23], Chong and Perry [24], and Lighthill [25]. Specifically, Perry and Steiner [26] applied the critical point theory to identify the sectional streamline patterns. These critical points identified sectional streamline patterns by analyzing the critical points such as nodes (foci or centers), saddles, bifurcation lines, and their combinations by depicting the separatrices, critical points, and alleyways. This approach reveals the features of flow structures for both the steady flow and the evolution of unsteady vortical behaviors. Hunt *et al*. [27] obtained a general formula (Eq. 1) for finding the correlations between nodes (including four-way nodes *N* and three-way nodes *N*′) and saddles (including four-way saddles *S* and three-way saddles *S*′) when flow moves around the entities.

https://doi.org/10.1017/jmech.2012.31 Published online by Cambridge University Press

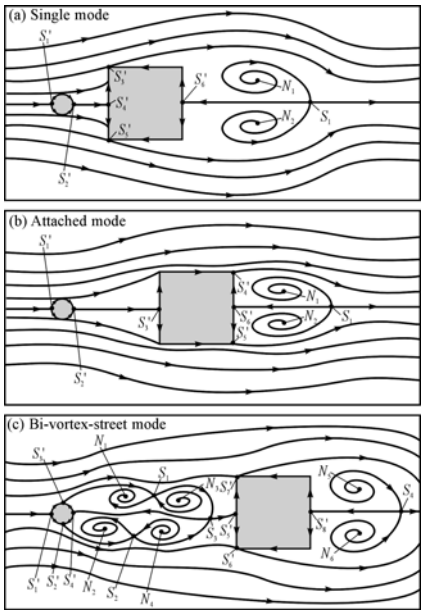


Fig. 7 Kinematic flow structures. (a) single mode at L/w = 1.0, (b) attached mode at L/w = 2.0 and (c) bi-vortex-street mode at L/w = 3.5

$$(\Sigma N + 1/2\Sigma N') - (\Sigma S + 1/2\Sigma S') = 1 - n \qquad (1)$$

where n is the connectivity of flow section. For instance, n = 1, 2, and 3 for none, one, and two entities in the flow field.

In the current study, the kinematic analysis is utilized to verify the smoke-streak and PIV flow patterns (Figs. 2 and 5) around the control rod and square cylinder were analyzed for various spacing ratios while Re = 3,715. Figure 7 displays the kinematic flow patterns using n = 3 while two entities are installed in the flow field. The critical nodes for each mode are listed as follows.

$\Sigma N = 2$, $\Sigma N' = 0$, $\Sigma S = 1$, and $\Sigma S' = 6$,
in single mode. (Fig. 7a)

$\Sigma N = 2$, $\Sigma N' = 0$, $\Sigma S = 1$, and $\Sigma S' = 6$,
in attached mode. (Fig. 7b)

$\Sigma N = 6$, $\Sigma N' = 0$, $\Sigma S = 4$, and $\Sigma S' = 8$,
in bi-vortex-street mode. (Fig. 7c)

These critical points in each mode satisfied the kinematic flow condition (Eq. 1).

Figure 8 shows the kinematic flow patterns obtained using various rotation angles and spacing ratios. These kinematic flow patterns were obtained from the smoke-streak and PIV flow patterns shown in Figs. 3 and 6, respectively. Figures 8(a) ~ (d) display the characteristic flow patterns for Modes I, II and III. In Modes I–III, the critical points are ΣN = 2, $\Sigma N'$ = 0, ΣS = 1 and $\Sigma S'$ = 6, which satisfy the kinematic flow condition (Eq. 1). Figures 8(e) and 8(f) show the vortex shedding occurring behind the upstream control rod (Modes IV and V). The critical points are ΣN = 6, $\Sigma N'$ = 0, ΣS = 4, and $\Sigma S'$ = 8. For each mode, the critical points satisfied the kinematic flow condition (Eq. 1).

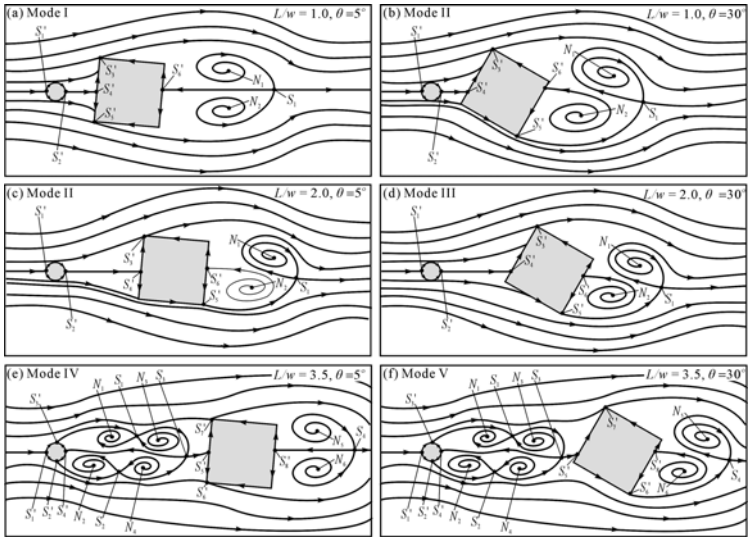


Fig. 8 Kinematic flow structures. (a) L/w = 1.0 at θ = 5°, (b) L/w = 1.0 at θ = 30°, (c) L/w = 2.0 at θ = 5°, (d) L/w = 2.0 at θ = 30°, (e) L/w = 3.5 at θ = 5°, and (f) L/w = 3.5 at θ = 30°

3.4 Wake-Flow Structures

The wake dimension adjacent to the square cylinder was utilized to identify the wake-flow characteristics. However, the wake dimension is a function of the projected width (d), where $d = w$ (cosθ + sinθ). The wake-flow frequency behind the square cylinder was normalized using the non-dimensional parameters – projected Reylonds number ($\mathrm{Re}_d = u_\infty d/\nu$), Strouhal number ($St = fw/u_\infty$), projected Strouhal number ($St_d = fd/u_\infty$), Roshko number [20] ($Ro = fw^2/\nu$), and projected Roshko number ($Ro_d = fd^2/\nu$). Equation 2 shows the relationships between St and Re (Eq. 2a) and Ro and Re (Eq. 2b) for the Kármán vortex behind a circular cylinder, which was proposed by Roshko [20].

$$St = 0.212\left(1 - \frac{12.7}{\mathrm{Re}}\right); \qquad (2a)$$

$$Ro = 0.212\,\mathrm{Re} - 2.7\,. \qquad (2b)$$

Accordingly, the maximum St for circular cylinder is 0.212.

Figure 9 plots the variations of St_d against Re_d (Figs. 9(a) ~ 9(d)) and Ro_d versus Re_d (Figs. 9(e) ~ 9(j)) by varying the spacing ratio and rotation angle. Figures 9(a) and 9(e) plot the distributions around the single-square cylinder. Additionally, Eq. (3a) reveals that St_d approximates the constant of 0.133 at θ = 0° while Re_d is high. The variation of St_d versus Re_d is consistent with the data reported by Okajima [3], Norberg [28], and Chen *et al*. [29]. Moreover, the curve of Ro_d versus Re_d at θ = 0° is regressed as listed in Eq. (3b).

$$St_d = 0.133\left(1 - \frac{0.04}{\mathrm{Re}_d}\right), \text{ at } \theta = 0°. \qquad (3a)$$

$$Ro_d = 0.133\,\mathrm{Re}_d - 0.01, \text{ at } \theta = 0°. \qquad (3b)$$

https://doi.org/10.1017/jmech.2012.31 Published online by Cambridge University Press

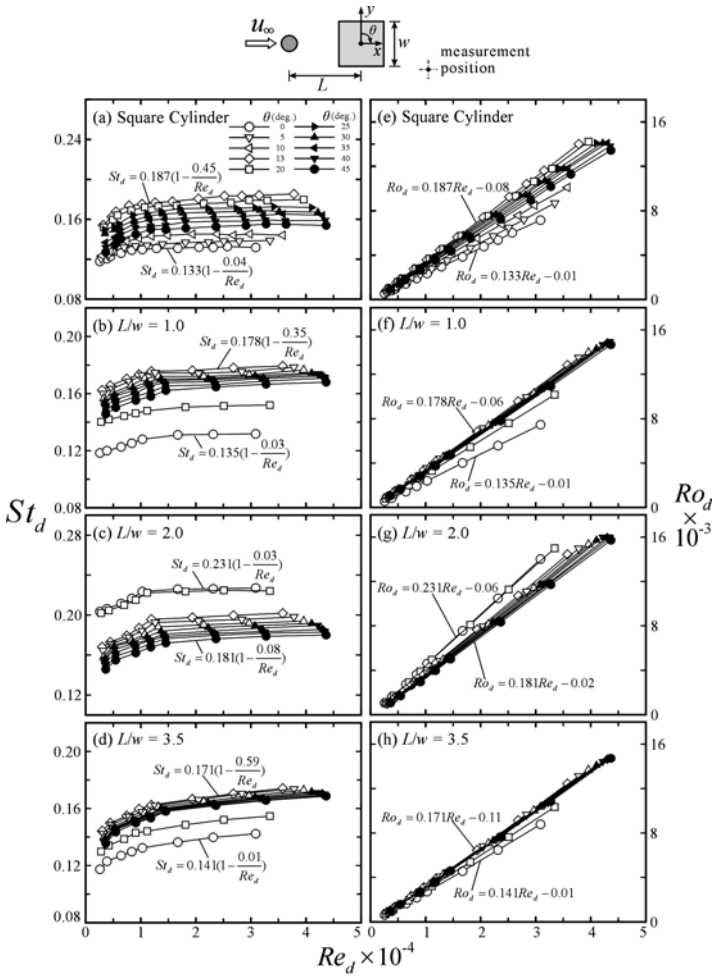


Fig. 9 Variations of projected Strouhal number (St_d) and projected Roshko number (Ro_d) against the projected Reynolds number (Re_d). (a) and (e): behind a single square cylinder. (b) and (f): L/w = 1.0. (c) and (g): L/w = 2.0. (d) and (h): L/w = 3.5

The maximum St_d of 0.187 occurs at θ = 13°. Accordingly, the maximum St_d approximates that obtained by Norberg [28], Chen *et al*. [29], and Knauss *et al*. [30]. Figures 9(b) and 9(f) plot the variations of St_d versus Re_d and that of Ro_d against Re_d in the single mode while L/w = 1.0. Moreover, the effect of θ on St_d is also considered. Figure 9(b) shows that 0.135 < St_d < 0.178 when 0° < θ < 45°. The minimum St_d of 0.135 occurs at θ = 0°, and the maximum St_d of 0.178 is at θ = 13°. Figures 9(c) and 9(g) plot the St_d–Re_d and Ro_d–Re_d curves, respectively, for attached mode when L/w = 2. The value of St_d is greater than 0.181 and less than 0.231, where the maximum St_d of 0.231 occurs at θ = 0° and the minimum St_d of 0.181 occurs at θ = 45°. Figures 9(d) and 9(h) delineates the distributions of St_d–Re_d and Ro_d–Re_d, respectively, for bi-vortex-street mode when L/w = 3.5. The St_d ranges from 0.141 to 0.171 using various rotation angles. Namely, the minimum St_d of 0.141 occurs at θ = 0° while the maximum St_d of 0.171 occurs at θ = 13°.

Figure 10 plots the distributions of St against Re and Ro against Re as θ = 0°. The relationships between St and Re and between Ro and Re behind the control rod were regressed as follows.

$$St = 0.212\left(1-\frac{0.04}{\mathrm{Re}}\right); \tag{4a}$$

$$Ro = 0.212\,\mathrm{Re} - 0.02\,. \tag{4b}$$

The maximum St behind the control rod is 0.212 while Re is sufficiently high. Accordingly, this result is consistent with the previous result [20] for a single-circular cylinder. Moreover, Fig. 10(a) displays that St behind the square cylinder exceeds that behind the control rod in the attached mode.

For the system of square cylinder with upstream control rod, the vortex-shedding frequency measured between the upstream control rod and square cylinder was denoted as St_1. Moreover, the vortex-shedding frequency detected behind the square cylinder is labeled as St_2. In the single mode, St_1 is lower than that behind the single-circular cylinder because the vortex shedding is restrained by the square cylinder. In the attached mode, St_1 is lower than that behind the single-circular cylinder while the vortex shedding is restricted by the square cylinder. In the bi-vortex-shedding mode, St_1 approximates that behind the single-circular cylinder since the square cylinder is far downstream. Table 1 summarizes the characteristics of St_1 and St_2. In the single mode, St_2 approximates that behind the single-square cylinder. That is, the vortex shedding is unaffected by the upstream control rod and the square cylinder dominates the flow characteristics in the single mode. Moreover, in the attached mode, St_2 approximates that behind the single-circular cylinder. Namely, the upstream control rod dominates the flow characteristics in the attached mode. In the bi-vortex-street mode, St_2 exceeds that behind the single-square cylinder and lowers that behind the single-circular cylinder. Namely, the upstream control rod dominates the flow characteristics in the bi-vortex-street mode. Additionally, Fig. 10(b) depicts the linear relationship between Ro and Re.

3.5 Surface Pressure, Drag and Lift

3.5.1 Distribution of Surface Pressure

The distributions of time-averaged surface pressure on the peripheries of square cylinder – on Faces *AB*, *BC*, *CD* and *DA* – were measured with a 32-tap pressure scanner transducer (Setra Co., Model 264, accuracy = ±1.0%). Figure 11 plots the curves of surface-pressure coefficient (C_p) along each face at Re = 1.25 × 10^4. Here, $C_p \equiv (p - p_{fs})/(0.5 \times \rho u_\infty^2)$, where p denotes the local static pressure on the cylinder surface, p_{fs} is the static pressure of free stream, and ρ is the air density.

Figure 11 shows the C_p profile around the single-square cylinder using various spacing ratios with θ = 0°. On Face *AB*, C_p is symmetrical about the stagnation point and the maximum C_p of 1.0 occurs at the stagnation point. Moreover, the minimum C_p of 0.72 occurs

https://doi.org/10.1017/jmech.2012.31 Published online by Cambridge University Press

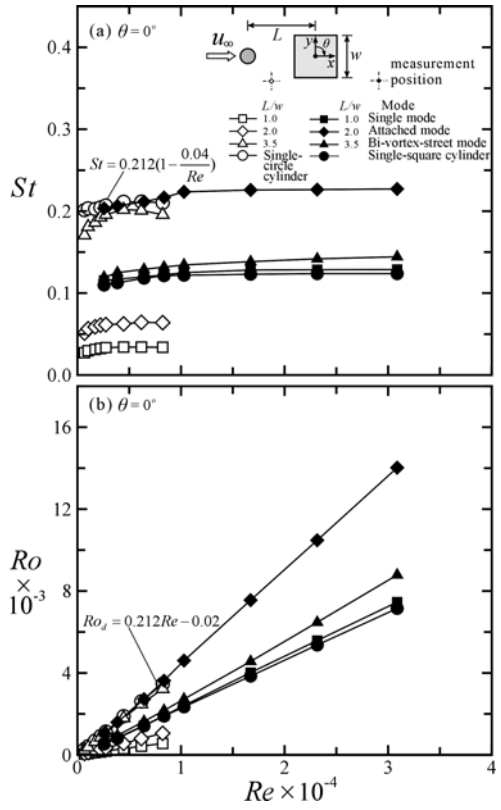


Fig. 10 Variations of (a) Strouhal number (*St*) versus Reynolds number (Re) at θ = 0° and (b) Roshko number (*Ro*) versus Reynolds number (Re) while θ = 0°, where the hollow circles represents *St* behind the control rod and solid circles denotes *St* behind the square cylinder

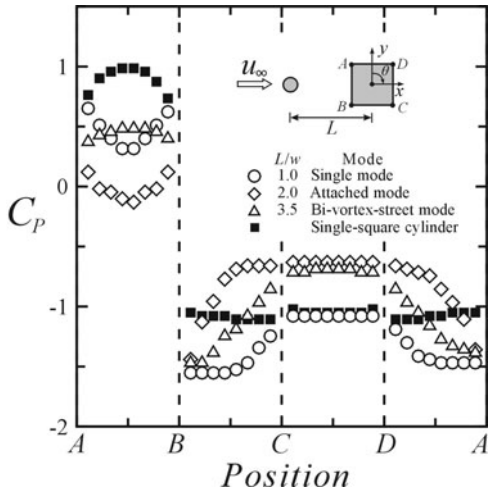


Fig. 11 Distributions of mean pressure coefficient (C_p) on the peripheral of square cylinders

at vertices *A* and *B*. However, in the single mode, the distribution of C_p on Face *AB* is symmetrical about the central point and the minimum C_p of 0.31 occurs at the central point. Namely, the presence of upstream control rod lowers C_p about 57%. Moreover, the maximum C_p of 0.65 occurs at vertices *A* and *B* in the single mode. In the attached mode, the distribution of C_p is symmetrical about the central point of Face *AB*. The maximum C_p of 0.12 occurs at vertices *A* and *B*, whereas the minimum C_p of −0.13 occurs at the central point of Face *AB*. In the bi-vortex street mode, the distribution of C_p is symmetrical about the central point of Face *AB* and the maximum C_p of 0.48 occurs at the central point. Additionally, the minimum C_p of 0.37 occurs at vertices *A* and *B* in the bi-vortex street mode.

The distribution of C_p on Face *BC* for the single-square cylinder and for the combination of square cylinder with control rod were discussed as follows. The distribution of C_p on the single-square cylinder declines from −1.1 (at vertex *B*) to −1.2 (at vertex *C*). However, in the single mode, C_p increased from −1.55 (at vertex *B*) to −1.24 (at vertex *C*). In the attached mode, C_p increased from −1.44 (at vertex *B*) to −0.66 (at vertex *C*). Furthermore, in the bi-vortex-street mode, C_p increased from −1.47 (at vertex *B*) to −0.85 (at vertex *C*). Specifically, the pressure coefficients on Face *CD* for each condition are almost constant. Namely, C_p is −1.05, −1.07, −0.63 and −0.69 for the single-square cylinder, single mode, attached mode and bi-vortex-street mode, respectively. Finally, the distributions of C_p for each mode on Face *DA* are the mirror symmetry to those on Face *BC*.

3.5.2 Drag and Lift

The C_p distributions were adopted to determine the mean drag coefficient (C_D) and mean lift coefficient (C_L). Equations (5) and (6) define C_D and C_L herein.

$$C_D = \left(\int_A^B C_p \cos\theta \cdot ds + \int_B^C C_p \sin\theta \cdot ds - \int_C^D C_p \cos\theta \cdot ds - \int_D^A C_p \sin\theta \cdot ds \right) / w$$

$$C_L = \left(-\int_A^B C_p \sin\theta \cdot ds + \int_B^C C_p \cos\theta \cdot ds + \int_C^D C_p \sin\theta \cdot ds - \int_D^A C_p \cos\theta \cdot ds \right) / w$$

Figure 12 plots the profiles of C_D and C_L against θ using various *L*/*w* at Re = 1.25 × 10^4. For comparison, Fig. 12 (a) also plots the experimental results obtained by Naudascher *et al.* [31]. Figure 12 (a) indicates that C_D is around 2.06 for the single-square cylinder at θ = 0°. Specifically, the value of C_D = 2.06 is consistent with C_D = 2.04 obtained by Naudascher *et al.* [31]. In the single mode, C_D of the square cylinder is 1.8, which is lower than 2.06 for the single-square cylinder due to the upstream control rod. In the bi-vortex-street mode, C_D of the square cylinder is 1.3, which is lower than 2.06 about 37%. In the attached mode, C_D of the square cylinder is 0.884 which is 57% lower than 2.06. Namely, the upstream control rod has a strong effect in the attached mode. In the attached flow mode, the upstream control rod changes the flow structures and vortex-shedding behaviors; and therefore, the surface pressure on the square cylinder is redistributed. Additionally, for a square cylinder with upstream control rod, the C_D curve indicates that the maximum C_D occurs at *L*/*w* = 1.0 and the minimum C_D occurs at *L*/*w* = 2.0 while θ is changed. Figure 12(b) reveals that the distributions of C_L versus θ using various spacing ratios. The

https://doi.org/10.1017/jmech.2012.31 Published online by Cambridge University Press

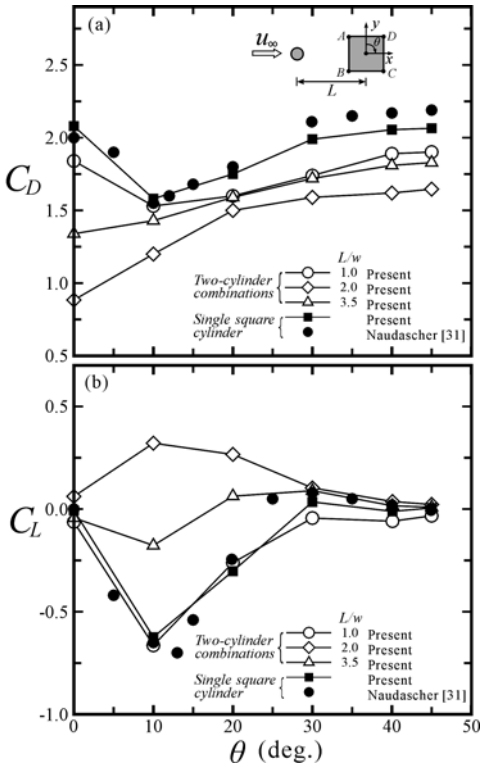


Fig. 12 Variations of (a) mean drag coefficient (C_D) against rotation angle (θ) and (b) mean lift coefficient (C_L) against the rotation angle (θ) while Reynolds number (Re) is 1.25×10^4

maximum C_L of 0.3 occurs at L/w = 2.0 while θ = 10° because of the pressure difference existing between Faces *BC* and *DA*. This pressure difference is generated when the shear layer separated from the upstream control rod. This separated shear-layer flow impinges on Faces *AB* and *BC*; and then induces a strong pressure disturbance (Fig. 3(d)). Additionally, the spacing-ratio negligibly affects C_L while θ > 30°.

4. CONCLUSIONS

This study investigated the flow patterns, vortex-shedding frequency and aerodynamic performance for the square cylinder with an upstream control rod using various rotation angles, Reynolds numbers and spacing ratios. Based on the results, the conclusions are listed as follows.

1. The smoke-streak patterns are categorized into three flow modes by varying Reynolds number and spacing ratio when rotation angle is 0°. The characteristic flow patterns are single, attached, and bi-vortex-street modes. Moreover, five different flow patterns — Modes I, II, III, IV and V — occurs when the rotation angle and spacing ratio are varied while Reynolds number is 3,715.
2. In the single mode, the Strouhal number behind square cylinder approximates that behind the single-square cylinder. The effect of upstream control rod on the flow patterns is negligible. In the attached mode, the Strouhal number behind the square cylinder is close to that behind the single-circular cylinder. Namely, the effect of upstream control rod on flow patterns is significant in the attached mode. Moreover, in the bi- vortex-street mode, the Strouhal number locates between those of single-square cylinder and single-circular cylinder. That is, the flow patterns are influenced by the upstream control rod.
3. In the single mode, the mean drag coefficient of the square cylinder is 1.8, which is lower than 2.06 behind the single-square cylinder due to the presence of upstream control rod. In the attached mode, the mean drag coefficient of the square cylinder is 0.884 which is about 57% lower than 2.06. Namely, the effect of upstream control rod is significant in the attached mode.

ACKNOWLEDGMENTS

This research was supported by the National Science Council of the Republic of China, under Grant No. NSC 97-2221-E-019-039.

REFERENCES

1. Gad-el-Hak, M., "Introduction to Flow Control," Eds.: Gad-el-Hak, M., Pollard, A., and Bonnet, J.-P., Flow Control: Fundamentals and Practices, Springer-Verlag, Berlin, pp. 1–153 (1998).
2. Gad-el-Hak, M., *Flow Control – Passive, Active, and Reactive Flow Management*, Cambridge University Press, New York, pp. 150–228 (2000).
3. Okajima, A., "Strouhal Numbers of Rectangular Cylinders," *Journal of Fluid Mechanics*, **123**, pp. 379–398 (1982).
4. Zdravkovich, M. M., "Review of Flow Interference between Two Circular Cylinders in Various Arrangements," *ASME Journal of Fluids Engineering*, **99**, pp. 618–633 (1977).
5. Yen, S. C., San, K. C. and Chuang, T. H., "Interactions of Tandem Square Cylinders at Low Reynolds Numbers," *Experimental Thermal and Fluid Science*, **32**, pp. 927–938 (2008).
6. Lesage, F. and Gartshore, I. S., "A Method of Reducing Drag and Fluctuating Side Force on Bluff Bodies," *Journal of Wind Engineering and Industrial Aerodynamics*, **25**, pp. 229–245 (1987).
7. Sakamoto, H., Tan, K. and Haniu, H., "An Optimum Suppression of Fluid Forces by Controlling a Shear Layer Separated from a Square Prism," *Journal of Fluids Engineering*, **113**, pp. 183–189 (1991).
8. Strykowski, P. J. and Sreenivasan, K. R., "On the Formation and Suppression of Vortex Shedding at Low Reynolds Numbers," *Journal of Fluid Mechanics*, **218**, pp. 71–107 (1990).
9. Zhang, P. F., Wang, J. J., Lu, S. F. and Mi, J.,

https://doi.org/10.1017/jmech.2012.31 Published online by Cambridge University Press

"Aerodynamic Characteristics of a Square Cylinder with a Rod in a Staggered Arrangement," *Experiments in Fluids*, **38**, pp. 494–502 (2005).
10. Sarioglu, M., Akansu, Y. E. and Yavuz, T., "Control of Flow Around Square Cylinders at Incidence by Using a Rod," *AIAA Journal*, **43**, pp. 1419–1426 (2005).
11. Lesage, F. and Gartshore, I. S., "A Method of Reducing Drag and Fluctuating Side Force on Bluff Bodies," *Journal of Wind Engineering and Industrial Aerodynamics*, **25**, pp. 229–245 (1987).
12. West, G. S. and Apelt, C. J., "The Effects of Tunnel Blockage and Aspect Ration on the Mean Flow Past a Circular Cylinder with Reynolds Number Between 104 and 105," *Journal of Fluid Mechanic*, **114**, pp. 361–377 (1982).
13. Yen, S. C. and Hsu, C. M., "Flow Patterns and Wake Structure of a Swept-Back Wing," *AIAA Journal*, **45**, pp. 228–236 (2007).
14. Mueller, T. J., "Flow Visualization by Direct Injection," Ed.: Goldstein, R. J., Fluid Mechanics Measurements, 2nd ed., Taylor & Francis, Washington DC, pp. 367–450 (2000).
15. Hinds, W. C., *Aerosol Technology*, John Wiley, New York, pp. 104–126 (1982).
16. Keane, R. D. and Adrian, R. J., "Theory of Cross-Correlation Analysis of PIV Images," *Applied Scientific Research*, **49**, pp. 191–215 (1992).
17. Keane, R. D. and Adrian, R. J., "Optimization of Particle Image Velocimeters Part I: Double Pulsed Systems," *Measurement Science and Technology*, **1**, pp. 1202–1215 (1990).
18. Abernethy, R. B., Benedict, R. P. and Dowdell, R. B., "ASME Measurement Uncertainty," *ASME Journal of Fluids Engineering*, **107**, pp. 161–164 (1985).
19. Levi, E., "A Universal Strouhal Law," *ASCE Journal of Engineering Mechanics*, **109**, pp. 718–727 (1983).
20. Roshko, A., "On the Development of Turbulent Wakes from Vortex Streets," *NACA Report*, **1191** (1954).
21. Bearman, P. B., "On Vortex Street Wakes," *Journal of Fluid Mechanics*, **28**, pp. 625–641 (1967).
22. Coles, D., "The Uses of Coherent Structures," *Aerospace Sciences Meeting*, Reno, Nevada, *AIAA Journal*, pp. 85–0506 (1985).
23. Perry, A. E. and Fairlie, B. D., "Critical Points in Flow Patterns," *Advances in Geophysics B*, **18**, pp. 299–315 (1974).
24. Chong, M. S. and Perry, A. E., "A General Classification of Three-Dimensional Flow Fields," *Physics of Fluids*, **2**, pp. 765–777 (1990).
25. Lighthill, M. J., "Laminar Boundary Layers," *Oxford University Press*, Cambridge, pp. 48–88 (1963).
26. Perry, A. E. and Steiner, T. R., "Large-Scale Vortex Structures in Turbulent Wakes Behind Bluff Bodies; Part 1: Vortex Formation," *Journal of Fluid Mechanics*, **174**, pp. 233–270 (1987).
27. Hunt, J. C. R., Abell, C. J., Peterka, J. A. and Woo, H., "Kinematical Studies of the Flows Around Free or Surface-Mounted Obstacles; Applying Topology to Flow Visualization," *Journal of Fluid Mechanics*, **86**, pp. 299–446 (1978).
28. Norberg, C., "Flow around Rectangular Cylinders: Pressure Forces and Wake Frequencies," *Journal of Wind Engineering and Industrial Aerodynamics*, **49**, pp. 187–196 (1993).
29. Chen, J. M. and Liu, C.–H., "Vortex Shedding and Surface Pressures on a Square Cylinder at Incidence to a Uniform Air Stream," *International Journal of Heat and Fluid Flow*, **20**, pp. 592–597 (1999).
30. Knauss, D. T., John, J. E. A. and Marks, C. H., "The Vortex Frequencies of Bluff Cylinders at Low Reynolds Numbers," *Journal of Hydronautics*, **10**, pp. 121–126 (1976).
31. Naudascher, E., Weske, J. R. and Fey, B., "Exploratory Study on Damping of Galloping Vibrations," *Journal of Wind Engineering and Industrial Aerodynamics*, **8**, pp. 211–222 (1981).

(Manuscript received February 20, 2011, accepted for publication August 8, 2011.)

https://doi.org/10.1017/jmech.2012.31 Published online by Cambridge University Press